

Properties and nature of Be stars^{★,★★,★★★}

24. Better data and model for the Be+F binary V360 Lacertae

A. P. Linnell¹, P. Harmanec^{2,3}, P. Koubský^{3,*}, H. Božić⁴, S. Yang^{5,*}, D. Ruždjak⁴, D. Sudar⁴, J. Libich^{2,3}, P. Eenens⁶, J. Krpata², M. Wolf², P. Škoda³, and M. Šlechta³

¹ Department of Physics and Astronomy, Michigan State University, E. Lansing, MI, 48824 and Affiliate Professor, Department of Astronomy, University of Washington, Seattle, WA 98195, USA
e-mail: linnell@astro.washington.edu

² Astronomical Institute of the Charles University, Faculty of Mathematics and Physics, V Holešovičkách 2, 180 00 Praha 8, Czech Republic

³ Astronomical Institute, Academy of Sciences, 251 65 Ondřejov, Czech Republic
e-mail: hec@sunstel.asu.cas.cz

⁴ Hvar Observatory, Faculty of Geodesy, Kačićeva 26, 10000 Zagreb, Croatia
e-mail: hbozic(dsudar,rdomagoj)@hvar.geof.hr

⁵ Department of Physics and Astronomy, University of Victoria, PO Box 3055 STN CSC, Victoria, B.C., V8W 3P6, Canada
e-mail: yang@uvastro.phys.uvic.ca

⁶ Dept. of Astronomy, University of Guanajuato, 36000 Guanajuato, GTO, Mexico
e-mail: eenens@astro.ugto.mx

Received 7 July 2005 / Accepted 15 May 2006

ABSTRACT

Aims. We include existing photometric and spectroscopic material with new observations in a detailed study of the Be+F binary V360 Lac.

Methods. We used the programs FOTEL and KOREL to derive an improved linear ephemeris and to disentangle the line profiles of both binary components and telluric lines. The BINSYN software suite (described in the paper) is used to calculate synthetic light curves and spectra to fit the *UBV* photometry, an *IUE* spectrum, blue and red ground-based spectra, and observed radial-velocity curves.

Results. The observations provide evidence of circumstellar matter in the system. The system model shows that the Be primary star is *critically rotating*, and that the synchronously rotating secondary star fills its Roche lobe. The primary star has a mass of $7.45 M_{\odot}$. Radial-velocity observations establish a mass ratio of 0.163. Light curve synthesis demonstrates that the observed light curves are controlled largely by tidal distortion and irradiation of the massive primary by the less massive secondary. Synthetic spectra fit both blue and red observed spectra with the exception of spectral lines affected by circumstellar matter in the system. The synthetic spectra allow for gravity darkening and are consistent with critical rotation of the primary. Synthetic spectrum fits to a dereddened *IUE* spectrum produce a calculated system distance of 512 pc. This distance is 2σ beyond the Hipparcos distance.

Key words. stars: emission-line, Be – binaries: close – binaries: spectroscopic – stars: fundamental parameters – stars: individual: V360 Lac

1. Introduction

Since Struve (1931) suggested that the envelopes of Be stars result from a rotational instability, students of Be stars have repeatedly returned to the question of how close the rotation of Be stars is to the condition of null equatorial gravity. The three major factors why no generally accepted answer to this question has been found are:

1. A lack of accurate, directly measured masses of Be stars;

* Guest investigator, Dominion Astrophysical Observatory, Herzberg Institute of Astrophysics, National Research Council of Canada.

** Also based on observations from Hvar, Ondřejov and San Pedro Mártir Observatories.

*** Full Table 3 and the spectrograms used in this investigation (in FITS format) are only available in electronic form at the CDS via anonymous ftp to cdsarc.u-strasbg.fr (130.79.128.5) or via <http://cdsweb.u-strasbg.fr/cgi-bin/qcat?J/A+A/455/1037>

2. The inclinations of the rotational axes of Be stars are usually unknown; and
3. Determination of the projected rotational velocities has not adequately treated the effects of limb and gravity darkening in rapidly rotating objects.

For a long time the general consensus has been that Be stars rotate at about 60–70 per cent of their critical speed (see, e.g., Porter & Rivinius 2003, and references therein). More recently, Townsend et al. (2004) and Frémat et al. (2005) argued that Be stars may actually be rotating much closer to critical rotation.

It is obvious that careful studies of suitably selected Be stars in binaries with known orbital inclinations may help to solve this long-standing problem. The danger is, of course, that binary interaction can represent an additional complication and one can question how representative results of such studies will be for the whole population of Be stars. However, since the number of known binaries among Be stars is growing steadily (see, e.g., the

Table 1. Journal of new *UBV* photoelectric observations of V360 Lac. Observing stations are identified by their file numbers used in the Praha/Ondřejov data archives (see column “File No.”) as follows: 1... Hvar 0.65-m reflector, EMI6256 tube; 4... Ondřejov 0.65-m reflector, EMI6256 tube; 30... San Pedro Mártir 0.84-m reflector, Cuenta-pulsos photon-counting photometer with RCA 31034 tube; 61... Hipparcos satellite H_p broadband photometry transformed to Johnson *V* and *B* magnitudes.

File No.	Epoch (RJD)	No. of obs.	HD comp. / check
4	45936.6–45993.5	2	214680/217101
61	47884.3–49037.0	114	all-sky
30	51055.8–51065.8	14	217101/214680
1	51066.5–51428.4	6	217101/214680
30	51843.7–51849.7	9	217101/214680
1	52098.6–52263.4	107	217101/214680
30	52200.8–52212.7	51	214680/217101
1	52488.4–52584.4	21	217101/214680
1	52536.5–52561.5	21	214680/217101
1	52856.5–52940.3	29	217101/214680
1	53255.4–53279.4	15	217101/214680

catalog by Harmanec 2001), such binary studies can at least be relevant to a large subgroup of Be stars that are members of binary systems. Notably, the recent estimates of the most probable properties of γ Cas by Harmanec (2002) and φ Per by Harmanec (2003) lead to the conclusion that both of these stars may be rotating at critical rotation. However, since the inclinations are not accurately known for these two objects, the conclusions are uncertain.

The situation is much better for V360 Lac. We have numerous new spectral and *UBV* observations of V360 Lac, of better quality than those available to Hill et al. (1997). Consequently, we decided to re-analyze the total data set of V360 Lac in an effort to derive better physical elements of the system.

The B2e star V360 Lac (14 Lac, HD 216200) is now known as a double-lined spectroscopic Be+F binary with an orbital period of 10^h08^m54^s – see Hill et al. (1997) (hereafter Paper 17). These authors modelled the light curve using a simple model of a disk, and derived the first basic binary properties. However Paper 17 gives no details concerning how the light curve solutions were obtained. Independently of the Hill et al. paper, Bossi et al. (1998) analyzed their own photometry and spectroscopy and argued that V360 Lac is neither an ellipsoidal variable nor an eclipsing binary.

2. Observations and data reductions

2.1. Photometry

The observational data used in this study consist of all data sets used in Paper 17 (cf. Table 3 there) plus new *UBV* observations secured at Hvar, Ondřejov and San Pedro Mártir (SPM hereafter) observatories and H_p photometry secured by the ESA Hipparcos satellite (Perryman et al. 1997). Basic information about the new observations is in Table 1. Throughout the paper we reference epochs in RJD (“reduced” Julian date), where

$$\text{RJD} = \text{HJD} - 2\,400\,000.0.$$

All Hvar, SPM and Ondřejov data were reduced with the program HEC22 (rel.14); this program uses non-linear transformation formulae – see Harmanec et al. (1994) for a detailed account of the observing and reduction procedures and

Table 2. Comparison and check stars used by various photometric observers of V360 Lac and their *UBV* magnitudes adopted here, based on the latest standardization of Hvar and SPM all-sky *UBV* observations.

Star	HD	<i>V</i>	<i>B</i> – <i>V</i>	<i>U</i> – <i>B</i>
10 Lac	214680	4 ^m 882	–0 ^m 203	–1 ^m 043
HR 8733	217101	6 ^m 171	–0 ^m 144	–0 ^m 802
2 And	217782	5 ^m 109	0 ^m 085	0 ^m 112
EN Lac	216916	5 ^m 605	–0 ^m 143	–0 ^m 837

Table 3. Individual *UBV* observations of V360 Lac. Data from individual stations are identified by their numbers in column “station”, identical to those given in Table 1, and filters are coded as follows: 3 = *V*, 4 = *B*, and 5 = *U*. Original (O) observations, smoothed values derived by the HEC13 program (C) and residuals after smoothing (O–C) are all tabulated.

RJD	O–C (mag.)	Weight	Station / Filter	O (mag.)	C (mag.)
41132.8955	–0.0332	1.0	13/3	5.913	5.9462
41132.9023	–0.0202	1.0	13/3	5.926	5.9462
41133.9282	–0.0062	1.0	13/3	5.940	5.9462
41133.9341	–0.0092	1.0	13/3	5.937	5.9462
41139.9194	.0242	1.0	13/3	5.970	5.9458
41139.9241	.0282	1.0	13/3	5.974	5.9458
41160.9246	.0324	1.0	13/3	5.977	5.9446
41160.9348	.0244	1.0	13/3	5.969	5.9446
41161.9265	.0034	1.0	13/3	5.948	5.9446
41161.9319	–0.0086	1.0	13/3	5.936	5.9446

Harmanec & Horn (1998) for the program and its detailed manual. The Hipparcos broad-band H_p magnitudes were transformed into Johnson’s *V* and *B* magnitudes using transformation formulae derived by Harmanec (1998) and adopting the following mean Hvar and SPM all-sky¹ values for V360 Lac:

$$B - V = +0^m.083 \quad \text{and} \quad U - B = -0^m.508$$

These agree very well with the original Johnson et al. (1966) values $B - V = +0^m.08$ and $U - B = -0^m.51$.

A special effort was made to derive improved *all-sky* values for all comparison stars used, employing carefully standardized *UBV* observations secured at Hvar and San Pedro Mártir observatories. Release 14 of HEC22 allows modelling of time variable extinction during the night, and this notably improves the accuracy of all-sky photometry. The new mean all-sky *UBV* values for all comparisons are collected in Table 2. They were added to the respective magnitude differences to obtain standard *UBV* magnitudes of V360 Lac.

Program HEC13, written by P. Harmanec², was used to remove long-term variations from the *UBV* data, discussed in Sect. 4.1. This program uses Vondrák’s (1969, 1977) smoothing technique. We used the smoothing parameter $\epsilon = 2 \times 10^{-17}$ applied to 10-day normals of original data. Note, however, that

¹ By “all-sky” we mean the *UBV* values directly derived from the seasonal and nightly transformation formulae, whose coefficients were derived via a multi-night fit to photometric standards distributed over the visible sky, rather than a comparison with photometric standards only near in the sky to the program star. Only good nights suitable for such all-sky photometry were used – see Harmanec et al. (1994) for details.

² The Fortran source version, compiled version and brief instructions how to use the program can be obtained via <ftp://astro.troja.mff.cuni.cz/hec/HEC13>.

after the fit is derived, HEC13 provides *individual* smoothed observations on the output. The processed *UBV* data, with long-term light variations removed, constitute the orbital light curves which we fit in this paper. For the convenience of future investigators, we publish all of our standardized individual *UBV* observations together with their HJDs in Table 3. For illustration, we reproduce a short section of Table 3 with the heading and a few first *V* observations. Note that both observed and smoothed data are tabulated and that these smoothed values are *not* the result of modelling described in this paper.

2.2. Spectroscopy

New electronic spectra used here consist of the following three data sets³

1. 1 spectrum was secured at the coudé focus of the Ondřejov 2-m telescope by PHar in 1999 on RJD 51472.3477. The detector was a Reticon 1872RF/30, with 15 μm pixels. A 830.77 grooves per mm grating gave a dispersion of 17.2 \AA mm^{-1} in the first order which translates into about 0.26 \AA per pixel. The spectrum covers the approximate wavelength range 6280–6720 \AA .
2. 14 spectra were secured in 2001–2002 (RJDs 52 132.7797–52 309.6070) at the coudé focus of the 1.22-m reflector of the Dominion Astrophysical Observatory (DAO hereafter) by PK and SY. The detector was DAO UBC-1 CCD, which is a Loral 4096 \times 200 thick device with 15 μm pixels. Using the 1200 grooves per mm grating, the reciprocal linear dispersion of 10 \AA mm^{-1} translates to about 0.14 \AA per pixel on the CCD. The spectra cover the wavelength range 6200–6700 \AA .
3. 4 blue (3450–5560 \AA) and 8 red (5820–8620 \AA) spectra were secured in 2002 (RJDs 52510.5522–52574.3601), and in 2001–2002 (RJDs 52119.5195–52574.3596), respectively, in the Cassegrain focus of the Ondřejov 2-m reflector with the two channel echelle spectrograph HEROS. This spectrograph has a resolution of about 20000 over the whole wavelength range and a linear dispersion ranging from 3.9 \AA mm^{-1} at 4000 \AA to 6.8 \AA mm^{-1} at $\text{H}\alpha$. (For more details on this instrument, see Kaufer et al. 1996 and Škoda & Škoda 2002.)

Initial reductions (bias subtraction, flatfielding and creation of 1-D frames) were carried out by SY in IRAF for the DAO spectra. Initial reduction of HEROS spectra were carried out by PŠ and MŠ in MIDAS using the customized echelle package written by A. Kaufer and O. Stahl (for details see Škoda & Šlechta 2002). The reduction produced wavelength calibrated extracted echelle orders. The echelle orders were unblazed by division by the extracted flat field orders, and then were merged into one long spectrum using a combination of order overlap regions. The merged spectrum then was rebinned, after heliocentric correction, into a linear scale with equidistant steps of 0.1 \AA/pixel . Reduction of the Ondřejov Reticon spectra and other spectra, rectification of the spectra, cosmic spikes removal, radial velocity (*RV* hereafter) measurements, and spectrophotometry were carried out by PH, JK and PK. The data processing used the SPEFO 1996 program, written by Dr. J. Horn (see Horn et al. 1996; and Škoda 1996). In particular, we measured *RVs* of a carefully selected set of telluric lines and applied additional corrections to ensure that all red spectra are on the same zero point in *RV* – see Horn et al. (1996) for details.

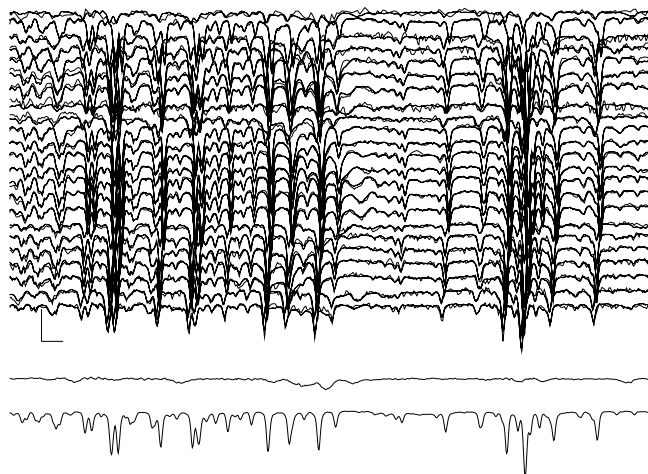


Fig. 1. KOREL disentangling of the spectrum of the secondary and telluric lines in the region from 6465 to 6529 \AA . The corresponding solution 1 is in Table 5.

3. Improving the ephemeris, known values of binary component masses, and spectroscopic separation of the stellar components

Reliable *RV* determinations for emission-line stars are difficult because of complications due to circumstellar matter (see Harmanec 2003 for a detailed discussion on this subject). In the particular case of V360 Lac, Hill et al. (1997) found that their *RV* curve of the Be primary is distorted near the phases of the *RV* maxima. This phenomenon, known as the Barr effect, is present in many emission-line binaries. The effect produces a false eccentricity with ω near 0° in an orbital solution, while the secondary star solution produces a circular orbit. The following section discusses our treatment of this problem.

3.1. KOREL disentangling

We used a recent version of program KOREL to disentangle the electronic spectra and to derive new orbital elements. See Hadrava (1995, 1997, 2004b).

We decided to use the largest data set of 23 red spectra covering the region from about 6300 to 6700 \AA and proceeded in the following steps:

1. We first extracted a data set for the wavelength region from 6465 to 6529 \AA (with a resolution of 2.9 km s^{-1}). This region contains a number of strong water vapour lines and also several lines of the secondary but no strong lines of the primary. Using this region, we obtained the first KOREL solution (solution 1 in Table 5). The solution determined the line strengths of the telluric lines in individual spectra and the orbital motion of the secondary.
2. We then adopted the line strengths of telluric lines from solution 1 and derived solutions for two other spectral regions, containing very weak telluric lines but strong lines of both binary components: region A (6329 to 6425 \AA with a resolution of 4.4 km s^{-1}), which contains the Si II 2 doublet, and region B (6620 to 6709 \AA with a resolution of 3.9 km s^{-1}), which contains the He I 6678 \AA line of the primary. The results are given as solutions 2 and 3 in Table 5, respectively.
3. To obtain *RVs* which could be combined with previous *RVs*, tabulated in paper 17, we averaged *RVs* of the primary and

³ These spectra are available at the CDS.

Table 4. Mean RVs of the primary and secondary from the KOREL solutions, derived via cross-correlation of the disentangled line profiles with the individual spectra.

RJD	RV ₁	RV ₂	Instrument
51472.3477	-20.36	22.45	Reticon
52119.5195	8.54	-137.15	HEROS
52202.4135	11.94	-127.26	
52213.3264	3.17	-60.10	
52510.5522	-29.90	60.55	
52525.5532	6.11	-96.82	
52527.5776	-28.04	83.86	
52530.5375	-22.71	84.75	
52574.3596	14.85	-168.86	
52132.7797	-5.0	-44.01	DAO
52132.9563	-2.60	-24.56	
52133.7187	-19.52	44.73	
52133.9867	-20.23	69.46	
52134.7254	-27.31	121.25	
52135.7324	-27.40	151.39	
52135.9723	-23.94	147.21	
52187.9218	-19.48	62.96	
52188.7860	-17.85	-23.21	
52189.7006	3.22	-106.05	
52190.9492	2.78	-166.03	
52191.7086	24.72	-155.17	
52287.6367	-31.36	138.17	
52309.6070	-26.05	-3.94	

secondary from solutions 2 and 3, after correcting for the γ velocities (see below). The RVs are listed in Table 4; the final solution is in Table 5.

KOREL derives individual RVs by cross-correlating the disentangled line profiles with individual observed spectra. By the way it operates, KOREL cannot derive the zero point of the velocity scale. It also does not provide error estimates of the orbital elements. An estimate of a γ velocity requires a direct RV measurement of the disentangled line profiles. By doing this, we find

$$\gamma_2 = -8.6 \pm 1.2 \text{ km s}^{-1}. \quad (1)$$

The value of γ_1 must be similar, but the complex shapes of the line profiles, including the emission contributions, prevent as reliable a determination as for the secondary star. We adopt the same γ velocities for both stars. We estimate the semiamplitudes of the RV curves and their rms errors as

$$K_1 = 25.7 \pm 2.0 \text{ km s}^{-1} \text{ and } K_2 = 157.8 \pm 1.0 \text{ km s}^{-1}, \quad (2)$$

which translates to

$$M_1 \sin^3 i = 5.55 M_\odot \text{ and } M_2 \sin^3 i = 0.906 M_\odot. \quad (3)$$

We believe the Table 4 RVs are relatively free of distortions due to emission. The KOREL solutions have an rms error per single observation of 4.7 km s⁻¹. The Table 4 RVs constitute our first data set. These velocities are heliocentric.

We have divided the paper 17 RVs into two groups: one for which we believe the observations are relatively free of distortion, and one which includes observations likely affected by distortions. The paper 17 RVs have an rms error per single observation of 6.7 km s⁻¹. By including the new observations of Table 4, our comparison with theoretical RVs treats the complete set of RVs as three separate data sets. Comparison of the observed radial velocities with the system model is in Sect. 7.

Table 5. Orbital solutions derived with KOREL (see the text for details). The orbital period was fixed at 10^d085408 derived in Paper 17. T_{sc} denotes the epoch of the superior conjunction in RJD-52 000.

Element	solution1	solution 2	solution 3	final solution
T_{sc}	284.434	284.443	284.467	284.447
K_1 (km s ⁻¹)	–	24.06	23.89	25.74
K_2 (km s ⁻¹)	158.05	158.04	159.43	157.79
M_2/M_1	–	0.152	0.150	0.163
γ_1 (km s ⁻¹)	–	–	–	-8.6
γ_2 (km s ⁻¹)	–	–	–	-8.6

3.2. Improved ephemeris

The mean epoch of the superior conjunction from the KOREL solutions of Table 5 is RJD 52 284.448 while the ephemeris used in Paper 17 predicts RJD 52 284.405. This discrepancy indicated that a small revision of the ephemeris is needed. We used the latest version of the computer program FOTEL, developed by Hadrava (1990, 2004a), to derive alternative orbital solutions from all existing RV data. FOTEL estimates the errors of the elements on the basis of a covariance matrix and allows determination of individual systemic velocities as elements of the solution.

A solution using all available primary and secondary RVs led to the following ephemeris:

$$T_{sc} = (\text{RJD } 52 \text{ } 284.447 \pm 0.014) + (10.^d085449 \pm 0.^d000027) \times E. \quad (4)$$

The epoch of the superior conjunction from ephemeris (4) agrees very well with the mean epoch from the KOREL solutions.

We tested the possibility of a secular change of the orbital period. Splitting the data into two time intervals, we obtained periods of (10^d08517 ± 0^d00042) and (10^d085500 ± 0^d000046) for the older and more recent RVs, respectively. Considering the associated errors, there is no compelling reason to assume a variable period on the basis of the available data. The result formally indicates a slow secular increase of the orbital period, as would be expected for a mass-exchanging system with a less massive and mass-losing secondary. Consequently, we derived a solution with \dot{P} as one of the elements. The solution was $\dot{P} = (1.75 \pm 2.5) \times 10^{-7}$ days per day. This is a non-significant result and we only use it to set an upper limit on the rate of mass transfer, assuming that the process is conservative, i.e. that no mass and angular momentum are lost from the system. For the masses derived here (see below), we find

$$\dot{M} \leq 3.2 \times 10^{-6} M_\odot \text{ yr}^{-1}. \quad (5)$$

Finally, we derived least-squares fits to all V , B and U photometric observations of V360 Lac, using the period from ephemeris (4) and its first harmonics. We found the following epochs of the deeper minima:

$$\begin{aligned} &\text{RJD } 52 \text{ } 284.440 \pm 0.005 \text{ in } V, \\ &\text{RJD } 52 \text{ } 284.379 \pm 0.004 \text{ in } B, \text{ and} \\ &\text{RJD } 52 \text{ } 284.145 \pm 0.008 \text{ in } U. \end{aligned}$$

This result, noted in Paper 17, suggests that a gas stream between the stars, or some other component of the circumstellar matter, affects the blue and ultraviolet light curves.

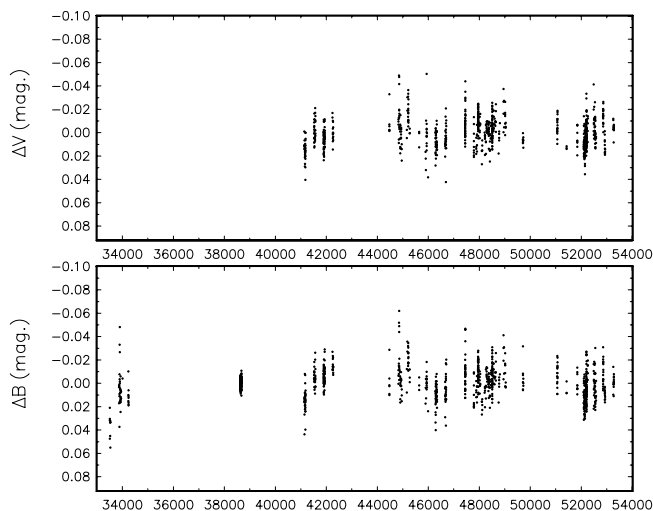


Fig. 2. A plot of V -band and B -band residuals from the orbital variations vs. RJD for all photometric data. Simultaneous cyclic variations in both bands are clearly present.

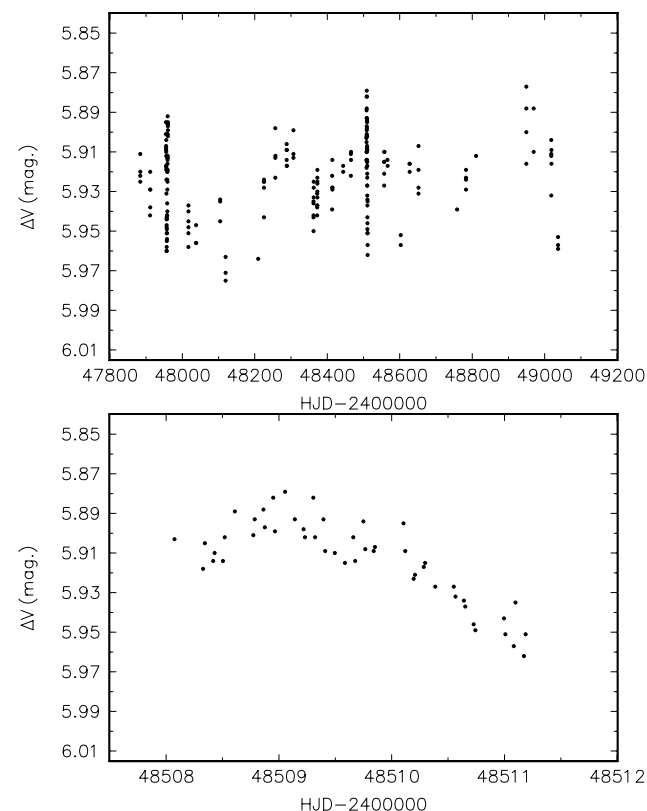


Fig. 3. A time plot of V -band residuals from the orbital variations for the Hipparcos data only: *Upper panel*: all data. *Bottom panel*: a subset demonstrating the presence of clear variations on a time scale of days.

4. Observed properties of the circumstellar matter

4.1. Photometry

Paper 17 showed that UBV light curves of V360 Lac exhibit “double-humped” light variation with an amplitude of a few hundredths of a magnitude. The light curves appear characteristic of a non-eclipsing system in which the light variation arises from effects of distortion and gravity darkening of a secondary star which fills or nearly fills its Roche lobe.

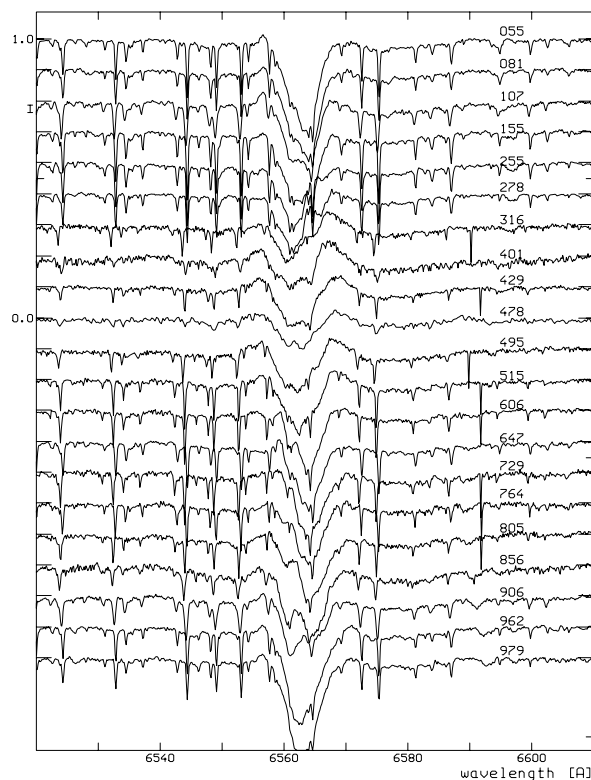


Fig. 4. Plot of $H\alpha$ profiles at 21 phases, from different orbital cycles. Note the phase-locked variation of V/R , with $V/R < 1$ in phases 0.3–0.4 and $V/R > 1$ in phases 0.7–0.8. The sharp, narrow absorption lines are due to the secondary star.

One of the conclusions of Paper 17 was that, in addition to the orbital light variations and their slightly different phase dependence at different wavelengths (discussed above), there are also mild cyclic or possibly periodic light changes on different time scales, one being 322 days. Long-term light variations are known for a number of Be stars (cf., e.g. Pavlovski et al. 1997). The new, standardised UBV photometry appears to confirm mild long-term variations of V360 Lac – see Fig. 2. Most of the photometric data were collected in short series, covering less than 0.06 d. We have not undertaken a more detailed characterization of the changes, such as with power spectral analysis.

To demonstrate that the variations are not caused by slight station-to-station differences and to understand their character better, we investigated the Hipparcos photometry alone (transformed to Johnson V). This data set is accurate and homogeneous and its advantage is that it does not suffer from the usual 1-d aliases. The plot of all Hipparcos V -band residuals vs. time gives an impression of systematic long-term changes – see the upper panel of Fig. 3. However, the scatter of individual data points indicates more rapid changes as shown in the bottom panel of the same figure. A period search in all V -band Hipparcos residuals finds a period of $9^{\text{d}}8147$, with a roughly sinusoidal light curve. This period is a 1-year alias of the orbital period; this variation may indicate that the amplitude of orbital light variations changes with time. An inspection of subsets of the photometric data gives the same impression. Dedicated, very accurate photometric observations will be needed to analyze this phenomenon more precisely.

4.2. Spectroscopy

We investigated the $H\alpha$ line profiles in all spectra. A sequence of these profiles, from different orbital cycles, is plotted in order of

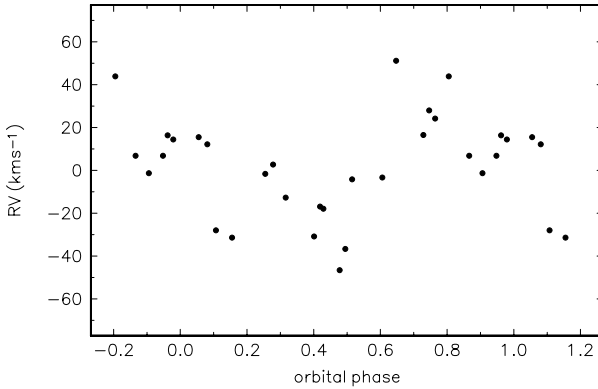


Fig. 5. Orbital RV curve of the H α emission wings.

orbital phases in Fig. 4. Both orbital and cycle-to-cycle changes are evident. We also measured RVs from these profiles. The RV curve of the H α emission wings is shown in Fig. 5. The emission wings *clearly follow* the orbital motion of the mass-gaining star. An orbital solution for these RVs gives $K_1 = 23.7 \pm 7.0 \text{ km s}^{-1}$, in excellent agreement with the KOREL solutions of Sect. 3.1.

Inspection of the H α profiles in Fig. 4 reveals phase-locked variation of V/R ($V/R < 1$ in phases 0.3–0.4, $V/R > 1$ in phases 0.7–0.8). This phenomenon is observed in many interacting and Be binaries (cf., e.g., previous papers of this series on 88 Her, 4 Her or V832 Cyg). Tomographic studies of some interacting systems (Geary & Richards 1996) show that the V/R changes are caused by a localized enhanced emission region between the components. A similar region was detected in the Be+F binary CX Dra (Richards et al. 2000) which is an analog of V360 Lac but with a lower inclination. The phase-locked variation is another piece of evidence indicating violation of axial symmetry in the distribution of circumstellar matter, discussed in Sect. 3.2.

5. Known system properties

The Hvar calibrated photometry gives

$$V = 5^m 91, B - V = 0^m 083, U - B = -0^m 508.$$

From standard relations (Becker 1963; Cox 2000) $Q = -0.570$, $E(B - V) = 0.270$, $E(U - B) = 0.189$, $A_V = 0.908$, giving $V_0 = 5.00$, $(B - V)_0 = -0.187$, $(U - B)_0 = -0.700$. Using the Hipparcos parallax, $M_V = -2.58$, with an estimated standard error of 0.50, arising from the uncertainty in the Hipparcos parallax.

Paper 17 shows that the primary star is rotating rapidly, with an equatorial $v \sin i \approx 200 \text{ km s}^{-1}$. Paper 17 also describes a cross-correlation function study of system spectra at both quadratures. Cross-correlation with a spectral type F8 mask produced sharp peaks due to the secondary star, establishing $T_{\text{eff},2} \approx 6000 \text{ K}$. This determination agrees with a separate spectral classification of F9 ± 1 spectral subclass (Paper 17). We estimate the limits on this temperature to be $\pm 200 \text{ K}$. (See Table 15.7 of Cox 2000.)

The primary star dominates the spectrum at optical wavelengths (Paper 17), and, based on the values of $(B - V)_0$, $(U - B)_0$, and Cox (2000), Table 15.7, the T_{eff} of the primary star is in the range 16 000 K to 20 000 K. Adopting $T_{\text{eff},1} = 18 000 \text{ K}$, Table 3 of Harmanec (1988) assigns a corresponding mass of $M_1 \approx 6.0 M_\odot$ and a radius of $R_1 \approx 4.0 R_\odot$. Given the value of $M_1 \sin^3 i$, Eq. (3), we expect a rough value $i \approx 85^\circ$.

The rapid rotation of the primary star suggests a mass transfer system in which the secondary star fills its Roche lobe.

Subsequent discussion in this paper demonstrates that the secondary star rotates synchronously. We believe that this condition, together with the rapid non-synchronous rotation of the primary star, constitutes clear evidence that the secondary star fills its Roche lobe.

The Hipparcos parallax of V360 Lac (Perryman et al. 1997) is $0''.00300 \pm 0''.00075$. The corresponding 2σ distance range is 222 pc to 667 pc.

6. Modelling software

All of our models are based on the BINSYN suite of programs (Linnell & Hubeny 1996). In the software package, a grid of points and associated photospheric segments defines the stellar photospheres. The software, in effect, interpolates a local synthetic spectrum at each photospheric segment to the local value of T_{eff} and $\log g$. The system synthetic spectrum then is calculated as the sum of the separate contributions, with proper allowance for Doppler shifts and other sources of line broadening. The interpolation takes place among arrays of source synthetic spectra for the two stars, individually calculated for single values of T_{eff} and $\log g$. The program assumes both stars are rigid rotators described by a Roche model.

A visibility key is associated with each segment on the stellar photospheres. For a given orbital phase and inclination, program routines determine whether a given segment is visible to the observer and appropriately set the corresponding visibility key. This information permits evaluation of eclipse effects. Each segment also receives a T_{eff} value appropriate to it, based on gravity darkening and irradiation for the stellar components. Program routines then integrate over each system component to calculate flux toward the observer, with due regard for visibility keys and the T_{eff} values and limb darkening of the individual segments. A final calculation sums the component contributions to provide a system flux toward the observer.

7. The system model

Using the approximate parameters from Sect. 5 and an initial test model, we calculated test V light curves and compared them with the observations. The test system showed deep eclipses, indicating that the value of i was too large.

Table 3 of Harmanec (1988) assigns the radius $R_1 \approx 4.0 R_\odot$ to a fairly large range of stellar masses. We preserved this test radius of the primary star while varying i and reached an inclination $i = 70^\circ$ for grazing eclipse. This exercise required recalculation of the primary star mass as i was changed, to preserve a fit to the radial velocity curves.

Using this preliminary model to compare with an observed spectrum we met a major problem. A section of the rectified spectrum, compared with observed spectrum BXN04816, is in Fig. 6. In this and subsequent plots that show spectra of individual components, flux has been added to those components to position them conveniently. This action has been necessary to make details visible that otherwise would be lost in a coarser ordinate scale. The contribution of the secondary star is much too large. However, the secondary star absorption line widths in the synthetic spectrum are in good agreement with the observed line widths. This feature confirms that the secondary star is rotating synchronously, and so supports the model in which the secondary star fills its Roche lobe.

Could the spectral contribution of the secondary star be reduced by an ad hoc assertion that the secondary star rotates synchronously but is smaller than its Roche lobe? In that case there

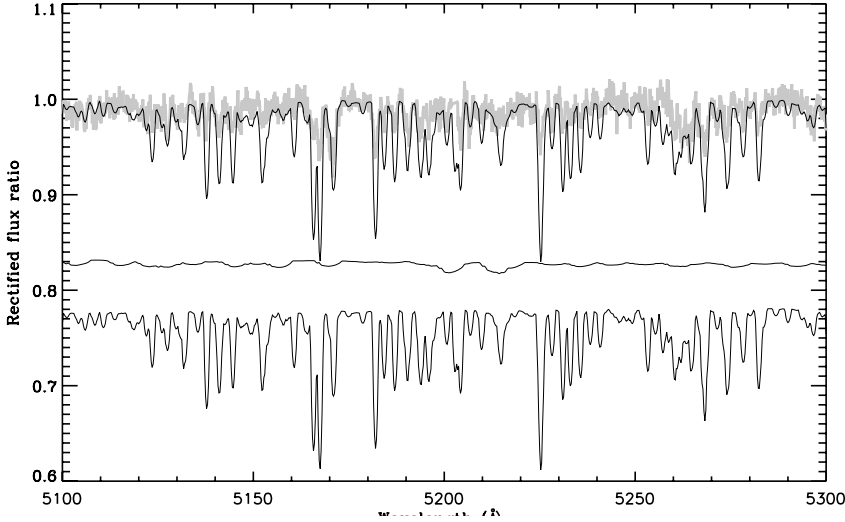


Fig. 6. Comparison of rectified synthetic system spectrum, for the preliminary model, with a portion of observed spectrum BXN04816. The continuous line at the top is the system spectrum, superposed on the observed spectrum (grey curve). The middle continuous line is the rectified primary star spectrum. This spectrum has been positioned by adding 0.36 to all ordinates. The bottom line is the rectified secondary star synthetic spectrum, positioned by adding 0.25 to all ordinates. Note that the contribution of the secondary star is much too large, so the preliminary model cannot be correct. See the text for details.

Table 6. System parameters used to simulate photometric observations and spectra for the system model.

Parameter	value	parameter	value
P (d)	10.085449	$\log g_1$ (pole)	3.55
\mathcal{M}_1 (\mathcal{M}_\odot)	7.45 ± 0.3	$\log g_1$ (point)	1.88
q	0.163 ± 0.005	$\log g_1$ (side)	2.53
Ω_1	5.50 ± 0.05	$\log g_1$ (back)	2.30
Ω_2	2.13791546	$T_{\text{eff},2}$ (pole)(K)	6000 ± 200
FV_1	6.19 ± 0.05 (est.)	$T_{\text{eff},2}$ (point)(K)	6599
FV_2	1.0	$T_{\text{eff},2}$ (side)(K)	5926
i ($^\circ$)	65.0 ± 1.0	$T_{\text{eff},2}$ (back)(K)	5661
D (R_\odot)	40.327	R_2 (pole) (R_\odot)	8.851
A_1	1.0	R_2 (point) (R_\odot)	13.037
A_2	0.70	R_2 (side) (R_\odot)	9.204
β_1	0.25	R_2 (back) (R_\odot)	10.496
β_2	0.08	$\log g_2$ (pole)	2.65
$T_{\text{eff},1}$ (pole)(K)	$18\,000 \pm 1000$	$\log g_2$ (point)	-6.85
$T_{\text{eff},1}$ (point)(K)	8175	$\log g_2$ (side)	2.59
$T_{\text{eff},1}$ (side)(K)	9998	$\log g_2$ (back)	2.34
$T_{\text{eff},1}$ (back)(K)	8753	δ (phase) ^a	-0.03
R_1 (pole) (R_\odot)	7.552		
R_1 (point) (R_\odot)	11.170		
R_1 (side) (R_\odot)	10.621		
R_1 (back) (R_\odot)	10.897		

^a Phase shift applied to synthetic light curves for optimum match to the observed V light curve. See text for details.

would be no credible explanation for the rapid rotation of the primary star. Moreover, if the secondary star once filled its Roche lobe and has subsequently detached from it, the secondary would not now rotate synchronously, by conservation of angular momentum. Can the secondary star fill its Roche lobe but the temperature of the primary star be increased appropriately? An increase in the primary star T_{eff} would produce a more discrepant fit to the *IUE* spectrum of the system, described below. Another alternative would be to reduce the secondary star T_{eff} . The T_{eff} of the secondary star cannot be reduced by a large amount without destroying the light curve fit described below. The absorption line strengths of the secondary star are temperature sensitive and reducing the secondary star T_{eff} actually tends to increase the intrinsic line strengths, counteracting the expected gain by reducing the secondary star T_{eff} . The direct way to reduce the secondary star contribution is to increase the size of the primary star while preserving its T_{eff} .

We increased the size of the primary star by reducing Ω_1 , without changing its polar T_{eff} , until the reduced relative spectral contribution of the secondary star matched the observed spectrum, as determined by eye estimate. The increased primary star radius required a reduction in i to 65° , and a corresponding increase in the primary star mass to preserve the radial velocity fit. The resulting model represents our system solution. The model parameters are in Table 6. Ω_1 and Ω_2 are Roche potentials, with Ω_2 set equal to the separately calculated Roche potential of the inner critical surface. FV_1 and FV_2 are rotation rates in units of synchronous rotation, A_1 and A_2 are bolometric albedos, β_1 and β_2 are gravity darkening exponents. The other parameters are self-explanatory. Equations for calculating gravity and other parameters are in Linnell (1984). The equator values of $T_{\text{eff},1}$ are gravity-darkened values for an equilibrium structure distorted by rapid rotation and tidally distorted by the companion. Our software uses the theory by Limber (1963) to represent the surface form of the primary star. The theory considers the general case of nonsynchronous rotation in the presence of tidal distortion by a companion star. The theory then develops what Limber terms the first approximation. In this approximation Coriolis forces and gas pressure gradients are neglected. Also neglected are radiation pressure and hydrodynamic effects such as Eddington-Sweet currents (Tassoul 1978). For the adopted Ω_1 , critical rotation occurs for $FV_1 = 6.1918755$. In view of the physical approximations of the theory, the Table 6 value of FV_1 corresponds to critical rotation. However, the adopted Ω_1 value depends on an eye estimate of the synthetic spectrum fit to the secondary star spectrum. It has an estimated uncertainty as shown in Table 6. A change in Ω_1 also changes the value of FV_1 for critical rotation; the uncertainty in FV_1 is dominated by the Ω_1 uncertainty.

Comparison of the primary star mass with main sequence values, Table 3 of Harmanec (1988) places the primary between spectral classes B1 and B2. The corresponding main sequence $\log T_{\text{eff}}$ values are 4.418 and 4.364. The polar $\log T_{\text{eff}}$ value for V360 Lac is 4.255, and allowing for temperature variation over the photosphere would reduce this to an average of about 4.17. The main sequence radii of B1 and B2 stars are $5.9 R_\odot$ and $4.21 R_\odot$, respectively. The Table 6 primary star polar radius of $7.552 R_\odot$ identifies this star as larger than a main sequence counterpart, and thus evolved. The $\log T_{\text{eff}}$ value is consistent with an evolved status.

The radial velocity fit for this model is in Fig. 7. The theoretical radial velocities are for the stars moving as mass points

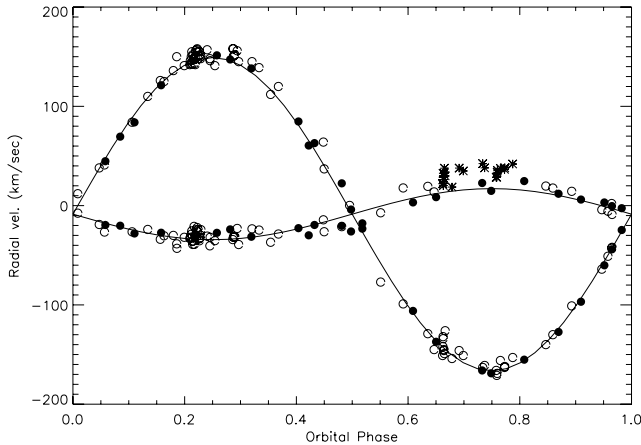


Fig. 7. Fit of theoretical radial velocities (RVs) to the observed velocities. The filled circles designate mean KOREL disentangled RVs , the open circles designate reliable RVs from paper 17, and the asterisks designate RVs from paper 17 that may be affected by emission lines and are less reliable.

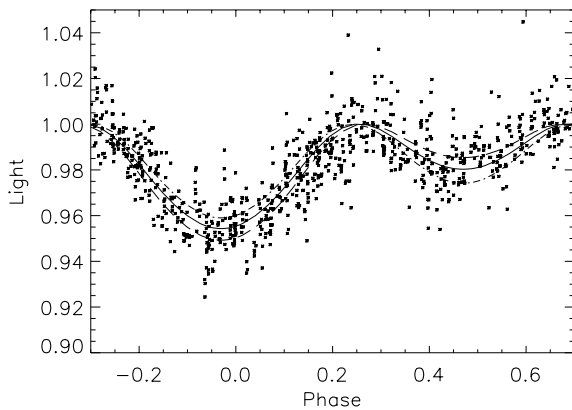


Fig. 8. Fit of three theoretical light curves to the observed V light curve. The solid line is for a secondary star bolometric albedo of 0.70, the dash line is for a bolometric albedo of 0.90, and the dot-dash line is for a bolometric albedo of 0.50.

in the center of mass system, with γ velocities added. Note that the plotted points are for three data sets. The standard deviation of the primary star velocity residuals from the first two data sets is 6.0 km s^{-1} and the standard deviation of the secondary star velocity residuals is 6.6 km s^{-1} . These standard deviations are of the same order as the corresponding quantities in the various solutions in Paper 17 and are consistent with the parameters determined in Sect. 3.1.

7.1. Synthetic light curves

The synthetic V light curve for the system model is sensitive to the primary star rotation parameter, FV_1 (see Table 6). Tidal distortion of the primary star by the secondary would be expected to be very small in view of the small mass ratio, as also would irradiation of the 18000 K primary by the 6000 K secondary. Rapid rotation of the primary, in isolation, produces distortion that is azimuthally constant, and so would have no effect on the light curve. Why, then, is the light curve sensitive to FV_1 ? We return to this point in later paragraphs.

Light curve sensitivity to the secondary star bolometric albedo is expected, and is present. The fit of the system model to the V light curve, for three values of the bolometric albedo, is

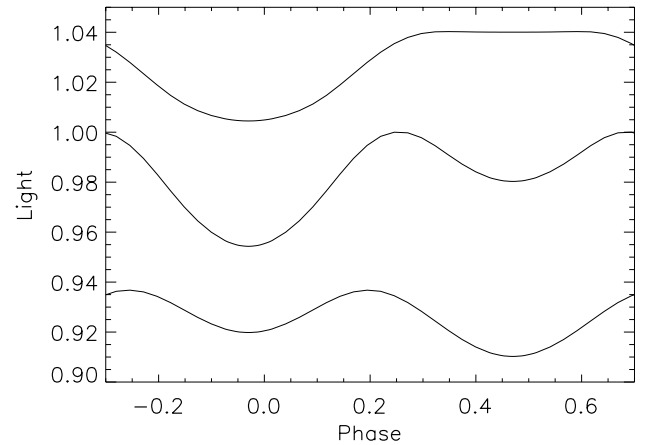


Fig. 9. Contributions of the separate stellar components to the V light curve, and the system V light curve. The top curve is the contribution of the secondary star, with 0.95 added to all ordinates. The bottom curve is the contribution of the primary star, with 0.02 added to all ordinates. It is rotating at 6.19 times the synchronous rate. The middle curve is the system V light curve. See the text for details.

in Fig. 8. In calculating these light curves we used a black body radiation curve at the local T_{eff} value of each photospheric segment. See Sect. 6 for further details. The synthetic light curves have been shifted -0.03 phase units for an optimum match to the observed light curve. The phase shifts applied to the synthetic light curves were produced by visual estimates. They are appreciably larger than the phase displacements corresponding to the epochs of the deeper minima in Sect. 3.2, using the first harmonics of the orbital period. This effect represents a phase difference between the KOREL radial velocity ephemeris and the observed light curves. We suggest it could be a light curve effect indicating lack of light symmetry of the actual system about orbital phase 0.0. The model assumes complete symmetry.

In Fig. 8 the best fit (solid) line is the theoretical light curve for a bolometric albedo of 0.70, not far from the theoretically-preferred value of 0.60, according to Claret (2001). The formal mean residual, for 834 observations and in light units, is 0.00456 and the standard deviation of the light residuals is 0.01163. Figure 8 shows outliers that are fairly discrepant, with a grouping of negative residuals before phase 0.0 and positive residuals immediately following, as well as a few large positive residuals near phase 0.3. Note that all of the light curve plots have ordinates in light units, not magnitude units.

A synchronously rotating primary star model produces a very discrepant V light curve. Rapid primary star rotation is necessary to produce an acceptable light curve fit; a plot of the light curve contributions of the individual stars is needed to understand why. The V light curve contributions from the separate stellar components and the system light curve are in Fig. 9.

As the primary star rotation rate increases, equatorial gravity becomes smaller and tidal effects due to the secondary star become relatively more prominent. The important consideration in the present context is the effect of gravity darkening. As Table 6 tabulates, the primary star equatorial T_{eff} values are of order 9000 K less than the polar T_{eff} , and there is appreciable temperature variation along the equator. In the absence of irradiation by the secondary star, the “point” T_{eff} of the primary would be 6869 K (compare with the Table 6 value), based on the $\log g_1(\text{point})$ value of Table 6.

As the bottom curve shows in Fig. 9, the primary star exhibits strong effects of ellipticity and irradiation. In Fig. 9,

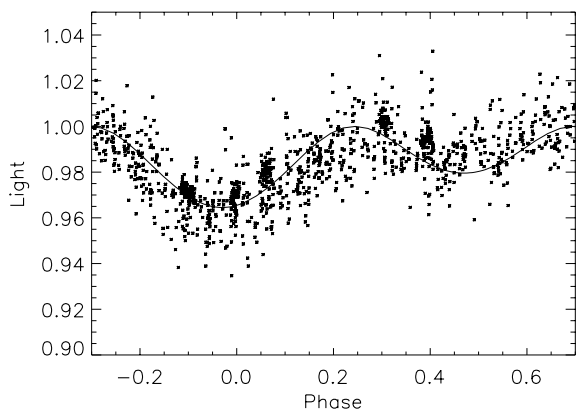


Fig. 10. Fit of the synthetic *B* light curve to observations.

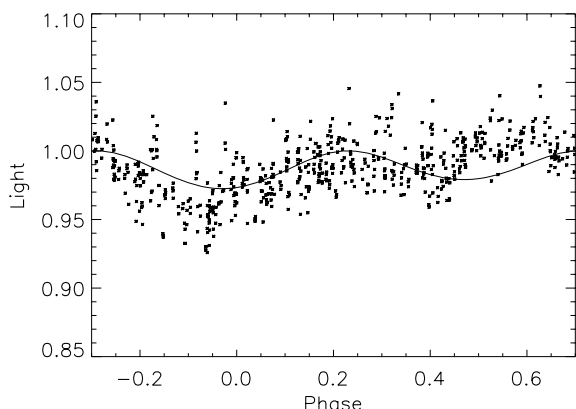


Fig. 11. Fit of the synthetic *U* light curve to observations. Note the change in ordinate range from the two previous light curve plots.

irradiation by the secondary star (including, importantly, the elevated secondary star inner face temperature produced by the primary star) causes the primary star brightness to be greater at orbital phase 0.0 than at phase 0.5. The upper curve, Fig. 9, shows the irradiation of the secondary star “point” by the primary, producing a constant brightness for an extended orbital phase around 0.5 rather than a minimum light at orbital phase 0.5. Note from the caption to Fig. 9 that 0.95 has been added to the secondary star ordinates. The secondary star contributes about 0.10 of the *V* system light. If the contributions were plotted without change on the Fig. 9 ordinate scale, Fig. 9 would have required more than the vertical height of a page. A coarser ordinate scale greatly reduces the visibility of the light variations. If the illumination by the primary star is reduced in an attempt to produce a double-humped secondary star light variation, the model quickly produces a too-bright secondary star, with too strong absorption lines in the synthetic spectrum. The system light curve is the resultant superposition of the two individual sources of light variation. Because of the important primary star contribution to the light curve, the optimum secondary star bolometric albedo of 0.70 does not represent a significant discrepancy from the theoretical value of 0.60. Fits to the *UBV* light curves, requiring the primary star to be at critical rotation, are a more sensitive test than a fit to the Balmer absorption lines. We stress that the system model fully accounts for gravity darkening. For a discussion of this point see Cranmer (2005).

The light curves used the limb darkening tables of Wade & Rucinski (1985), interpolated to the local photospheric values of T_{eff} and $\log g$. The adopted effective wavelength of the *V* band was 5500 Å. We have iterated the irradiative

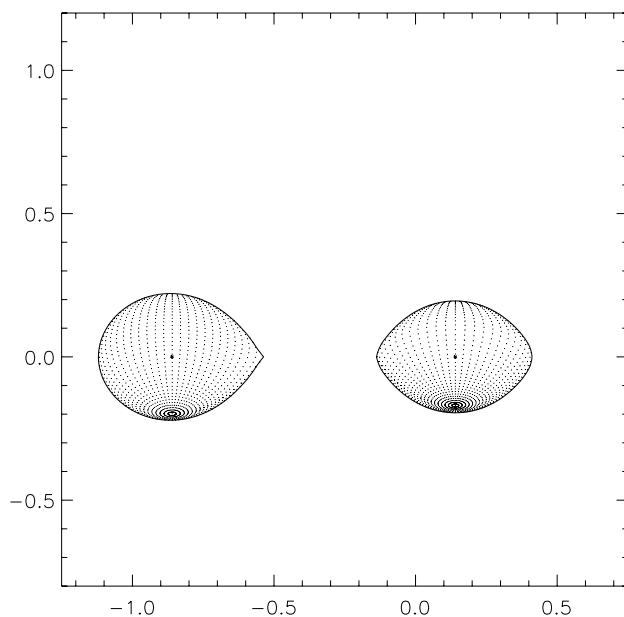


Fig. 12. View of system model projected on the plane of the sky, at orbital phase 0.25. The secondary star fills its Roche lobe. Rotational distortion is easily visible for the primary star. It rotates at 6.19 times synchronous rate. The unit of distance for both axes is the semi-major axis of the relative orbit.

interaction twice, in accordance with the prescription of Wilson (1990). Table 6 includes estimated errors of system parameters. The value listed for $T_{\text{eff},2}$ (pole) is the nominal value from Paper 17.

The model fit to the *B* light curve, calculated for an effective wavelength of 4340 Å, is in Fig. 10. The secondary star bolometric albedo is 0.70. The mean residual, for 1172 observations, is 0.00444, in light units, and the standard deviation of the residuals is 0.01151.

The model fit to the *U* light curve, calculated for an effective wavelength of 3650 Å, is in Fig. 11. The secondary star bolometric albedo is 0.70. The mean residual, for 620 observations, is 0.00798, in light units, and the standard deviation of the residuals is 0.01982.

A projection view of the system model, at orbital phase 0.25, is in Fig. 12. Rotational distortion of the primary star is easily visible. An important point from this analysis is that the primary star is at critical rotation. The term “critical rotation” requires some discussion. In the case of single stars, critical rotation means such small equatorial gravity that matter may be ejected by, e.g., radiation pressure. Gravity is constant along the equator in single stars. In the present case, the presence of the companion modifies the physical situation. If the primary star rotates synchronously, tidal distortion by the secondary star is nearly negligible. As the model primary star rotates faster, the fixed tidal distortion by the secondary becomes a larger contributor to the decreasing primary star equatorial gravity. Eventually, for sufficiently fast primary star rotation, “gravity” at the substellar equatorial point on the primary star goes to zero, while gravity at other equatorial points remains larger than zero. By “gravity” we mean net force directed inward, including gas pressure, radiation pressure, etc. This condition defines “critical rotation”.

Our analysis demonstrates that V360 Lac is a new example of the exotic morphological type first discussed by Wilson (1979) and termed “double-contact binaries”. See also the discussion of the double-contact system RZ Scuti

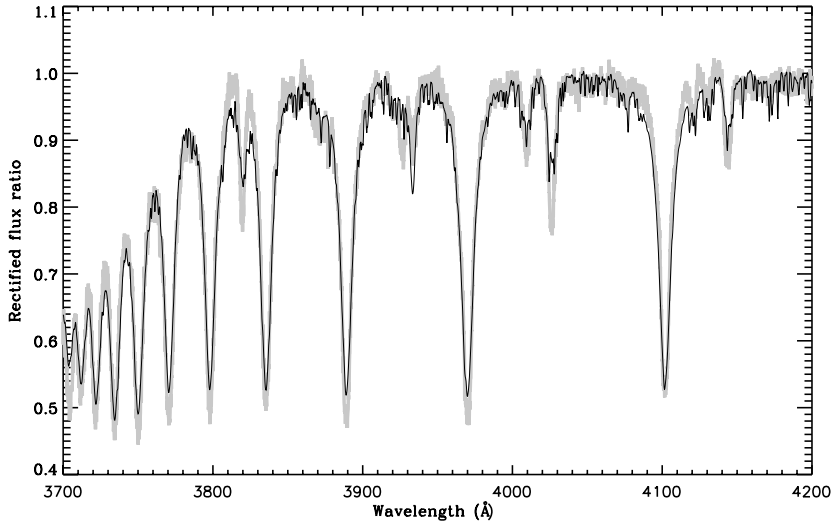


Fig. 13. Fit of system model synthetic spectrum (thin line) to observed (grey curve) spectral region including Balmer lines. The synthetic spectrum fit is reasonably good, including the fits to the $\lambda 3819$, $\lambda 4009$, $\lambda 4026$, and $\lambda 4144$ He I lines.

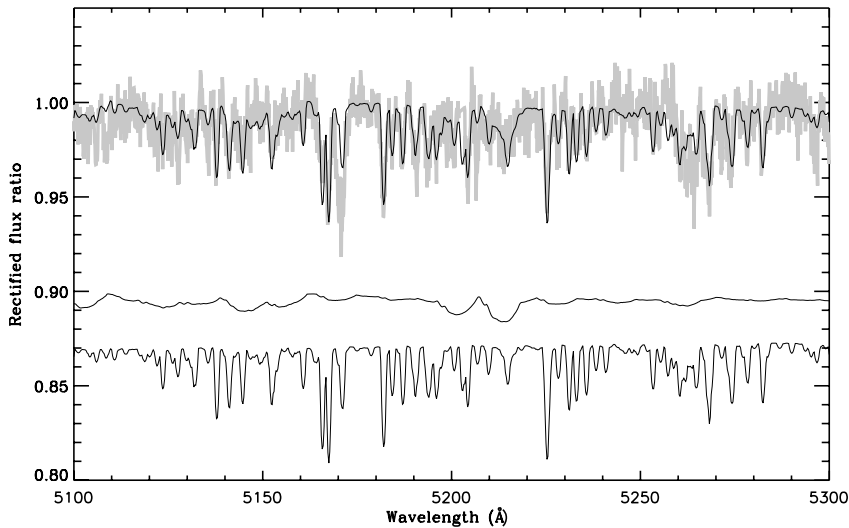


Fig. 14. Fit of rectified synthetic spectrum (thin line, top), for system model, to observed spectrum BXN04816 (grey curve). The primary star spectrum has been positioned by adding 0.10 to all ordinates, and the secondary star spectrum has been positioned by adding 0.67 to all ordinates. The synthetic spectrum identifications are as in Fig. 6, but note the different ordinate scale. Note the generally accurate fit of the secondary star lines to the observations. The fit demonstrates that the secondary star is rotating synchronously. Also note the smearing of the primary star lines that results from rapid stellar rotation.

(Wilson et al. 1985) and the review article by Wilson (1994). V360 Lac differs from RZ Scuti in that RZ Scuti is an eclipsing system.

7.2. Synthetic spectra

We used Kurucz (1993b) model atmospheres, with the Hubeny program SYNSPEC (v48) (Hubeny et al. 1985), to calculate synthetic spectra, at steps of 1000 K between 7000 K and 18 000 K, and for $\log g$ values of 2.5, 3.0, and 3.5 for each T_{eff} . This set of source spectra was used with the primary star. We also calculated synthetic spectra at T_{eff} values of 8000 K, 7000 K, 6000 K, 5000 K, and 4000 K and for $\log g$ values of 1.5, 2.0, 2.5, and 3.0 for the secondary star. Comparison of these $\log g$ values with the corresponding values in Table 6 shows that only very small regions on the two stars fall outside the tabulation ranges of the source spectra. If a photospheric segment has a T_{eff} or $\log g$ outside the tabulation range, BINSYN uses the nearest tabular entry. Since the outside-range values are at very small $\log g$ values, the corresponding photometric segments are subject to large gravity darkening, and the error in the flux value from using the nearest tabular $\log g$ produces a negligible error. All spectra were

calculated at a wavelength resolution of 0.1 Å. We adopted solar composition (the SYNSPEC default) in all calculations. The source synthetic spectra tabulate flux as function of wavelength. In calculating a system synthetic spectrum, BINSYN associates each source spectrum with a limb darkening coefficient. We have used a standard value of 0.6 and a limb darkening law of the form $I(\mu) = I(1)[1 - u(1 - \mu)]$, where u is the limb darkening coefficient and μ is the cosine of the angle between the surface normal and the line of sight.

All observed spectra have been rectified. BINSYN produces synthetic spectra with absolute flux calibrations and so must be rectified for comparison with the observed spectra. To rectify the synthetic spectra, we repeated the spectrum synthesis calculation but with continuum spectra substituted for the source synthetic spectra. (A given SYNSPEC run produces both a synthetic spectrum and a continuum spectrum.) We then divided the output produced with the regular source spectra by the output produced with the continuum spectra, giving a rectified synthetic spectrum. While this procedure gave results that fitted the rectified observed spectra well longward of 3800 Å, the rectified synthetic spectrum required small adjustment short of that wavelength to produce a close fit to the rectified observed spectrum.

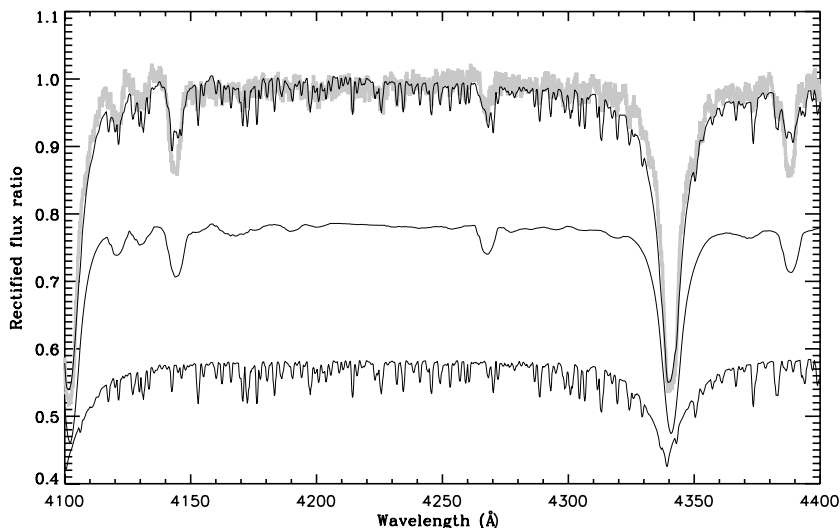


Fig. 15. Fit of model synthetic spectrum (thin line, top) to observed (grey curve) spectral region including H γ . This spectrum is at orbital phase 0.91. The spectrum of the primary star is in the middle and that of the secondary star is at the bottom. The spectrum of the primary star has been positioned by adding -0.03 to all ordinates, and the spectrum of the secondary has been positioned by adding 0.40 to all ordinates.

The fit of the rectified system synthetic spectrum to a portion of observed spectrum BXN04816 is in Fig. 14. This is the same observed spectrum as in Fig. 6. Note the difference in the ordinate scales. There now is a very good fit to many of the lines from the secondary star. This fit certifies that the secondary star is rotating synchronously. More rapid rotation would smear out the synthetic spectrum lines, while less than synchronous rotation would produce narrower synthetic spectrum lines.

Figure 13 shows the synthetic spectrum fit in a spectral region that includes several Balmer lines. The synthetic spectrum Balmer lines are slightly too shallow for the high series members. The secondary star $\lambda 3934$ Ca II line is prominent. The secondary star $\lambda 3968$ Ca II line blends with the primary star He line.

Figure 15 shows a different spectral region. The fit to the depth of the H γ line is quite good. Note the orbital Doppler displacement of the secondary star from the primary and the intermediate location of the system line, representing an average of the separate contributions.

The depths of the Balmer lines in the model are sensitive to the rotation parameter FV_1 . A too small FV_1 produces model Balmer lines deeper than observed. In principle, it would be possible to determine FV_1 by optimizing the fit to the depths of the Balmer lines. However, as Fig. 15 shows, the quality of fit is not a uniform function of the Balmer series members. We have chosen to use the light curve dependence on FV_1 to determine the best value of that parameter.

We now show fits to red spectra at three orbital phases, together with views of the system. The first group is at orbital phase 0.44, Figs. 17 and 18. A view of the system is in Fig. 16. The observed spectrum contains a number of narrow telluric lines near 6300 \AA and near 6500 \AA . The H α emission line, with its central reversal, is slightly displaced to the blue relative to the system synthetic spectrum absorption line, but aligns accurately with the absorption line in the synthetic spectrum of the primary star. This result is in agreement with the separately measured radial velocities of the emission wings described in Sect. 4.2. The far redward wing appears to be slightly in emission. Also note the emission wings of the primary star Si II and He I lines. The rotational broadening of the primary star lines is apparent. Figure 18 shows a detail of Fig. 17. The Doppler shifts of the secondary star lines are apparent by their displacements from

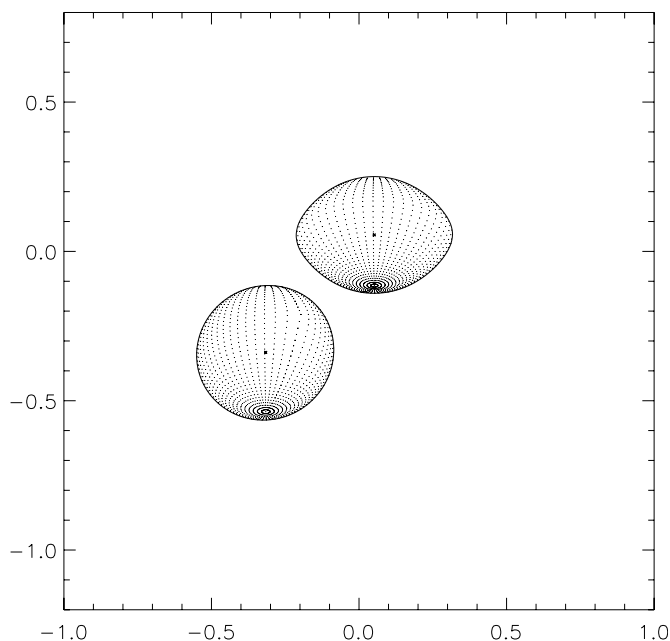


Fig. 16. View of V360 Lac model at orbital phase 0.44. The orbital inclination is 65° . The irradiated inner face of the secondary star is turned toward the observer. Note the rotational distortion of the primary star. This view is associated with the spectra in Figs. 17 and 18.

the line identification markers. Although the synthetic spectrum represents the secondary star reasonably accurately, there are some differences. Note the much stronger observed Si II features at 6347.1 and 6371.4 \AA than appear in the synthetic spectrum.

Figure 19 shows the system at orbital phase 0.50, nearly the same phase as Fig. 16. The Fig. 17 spectrum was taken at RJD 52187.9218, and the Fig. 20 spectrum was taken at RJD 52309.6070. The H α emission line continues to follow the primary star. Compare the orbital phase 0.50 Fig. 21 detail spectrum with Fig. 18 at orbital phase 0.44. The synthetic spectrum shows subtle changes, even over the short phase interval. The changes in the observed spectrum are different and larger, indicating temporal variation. Note in particular the changes in the Si II lines and the Fe I 6400.0 \AA line.

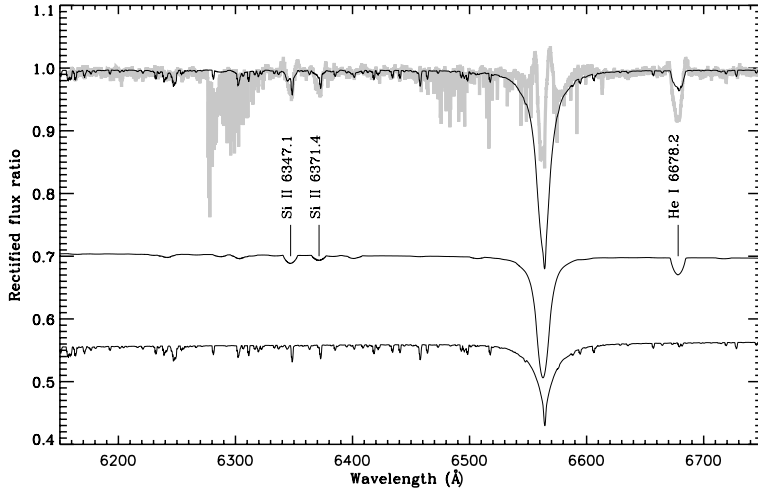


Fig. 17. Synthetic spectrum (thin line, top) compared with observed spectrum V3L14818 (grey curve) at orbital phase 0.44 (see Fig. 16). The middle spectrum is the primary star and the bottom spectrum is the secondary star. The primary star spectrum has been positioned by adding -0.11 to all ordinates, and the secondary star spectrum has been positioned by adding 0.37 to all ordinates. Note the decreasing contribution of the primary star and the increasing contribution of the secondary star with wavelength. Also note the $H\alpha$ emission with the central absorption reversal. The absorption component agrees with the wavelength of the primary star $H\alpha$ line, which is slightly displaced from the wavelength of the composite system synthetic spectrum.

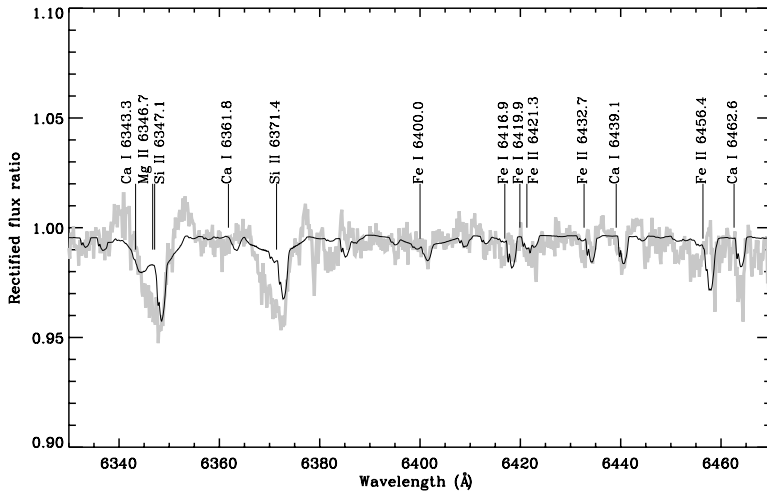


Fig. 18. Detail of Fig. 17. The Doppler shift of the secondary star spectral lines is clearly evident, since the line identification annotations are positioned at their listed wavelengths. Note the emission wings on the Si II doublet. As with $H\alpha$, the emission follows the motion of the primary star and indicates the presence of circumstellar matter associated with the primary star. The contribution of the rotationally-broadened primary star absorption lines is small (see Fig. 17). The strong Si II absorption components must be produced by circumstellar matter.

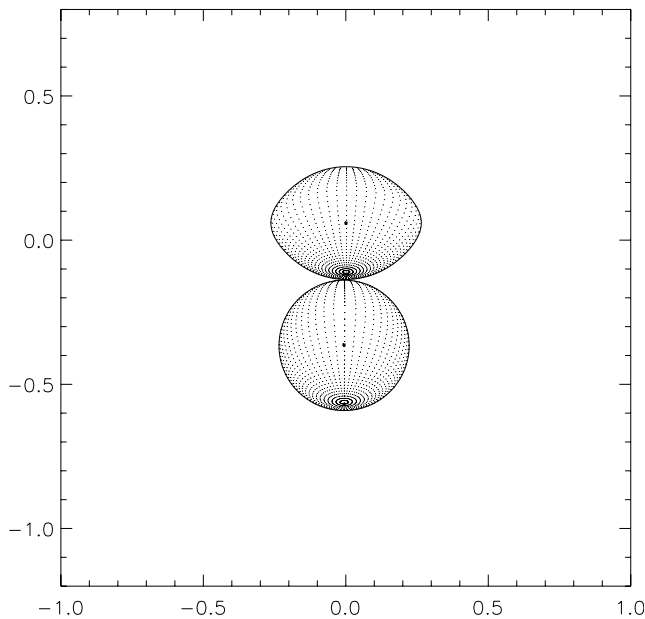


Fig. 19. View of V360 Lac model at orbital phase 0.50. Compare with Fig. 16. This view is associated with the spectra in Figs. 20 and 21. The primary star is nearer the observer and the observer sees the irradiated inner face of the secondary.

Figure 22 shows the system at orbital phase 0.98. The Fig. 23 spectrum was observed at RJD 52132.9563. In Fig. 23, note the greatly increased depth of the $H\alpha$ absorption reversal. In Fig. 24, note the appreciable changes, in both the observed and synthetic spectrum, from Fig. 21, especially the stronger absorption line features. If any mass transfer stream exists, it would appear projected on the disk of the primary star. We suggest that these enhanced absorption features may be associated with a mass transfer stream.

A single *IUE* spectrum of the system is available (SWP09204) to download from the *IUE* archive. Comparison of an initial system synthetic spectrum with one of the ground-based blue spectra, e.g. BXN04612, shows that the contribution of the secondary star is a few percent, at most, in the wavelength range $\lambda 3800$ to $\lambda 5300$. At *IUE* wavelengths the contribution of the secondary star is negligible. We used *IUEDAC* software to produce a dereddened spectrum, by application of the Savage & Mathis procedure (1979), followed by recalibration by the Massa & Fitzpatrick procedure (2000). We subjected the synthetic spectrum to Gaussian FWHM broadening to 5.0 \AA , using the Hubeny program ROTIN3 (Hubeny et al. 1985), to correspond to the resolution of the *IUE* spectrum.

The fit of this model to the *IUE* spectrum is in Fig. 25. The *IUE* spectrum is in physical flux units at the Earth. The system synthetic spectrum represents an integration over the

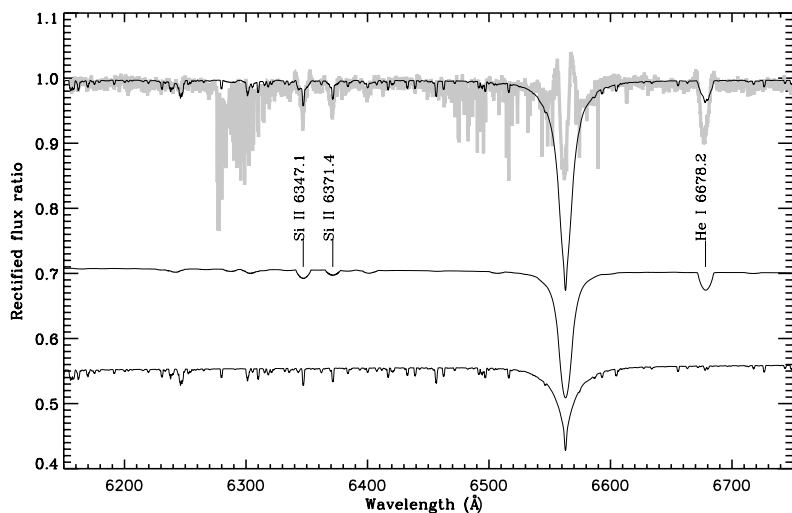


Fig. 20. Synthetic spectrum (thin line, top) compared with observed spectrum V3L00848 (grey curve) at orbital phase 0.50 (see Fig. 19). Spectra as in Fig. 17. The $H\alpha$ lines of the two stellar components and the central absorption reversal of the observed spectrum align more accurately at this orbital phase. The primary star spectrum has been positioned by adding -0.11 to all ordinates, and the secondary star spectrum has been positioned by adding 0.37 to all ordinates.

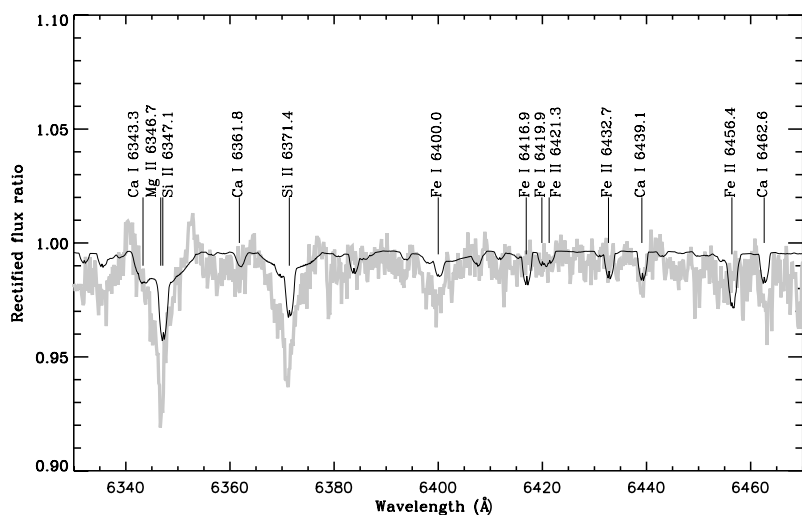


Fig. 21. Detail of Fig. 20. Note the subtle changes, in both the observed and synthetic spectrum, from Fig. 18. The Si II emission wings are present, as in Fig. 18, but the observed absorption component is deeper and narrower.

visible photospheres, and is expressed in physical flux units of $\text{erg s}^{-1} \text{cm}^{-2} \text{\AA}^{-1}$, evaluated at the star. We determine an empirical scale factor, S , applied to the synthetic spectrum, to superpose the two spectra.

If the distance to V360 Lac, in cm, is D , then $D^2 = S$. Superposition of the two spectra corresponds to a distance, formally, of 512 pc. This distance is slightly less than two standard deviations larger than the Hipparcos distance of 333 pc, which corresponds to a distance of 667 pc. The fit is reasonably good but the synthetic spectrum is slightly too hot. If our $E(B - V)$ value were slightly larger, the dereddened *IUE* spectrum would be a better fit to the synthetic spectrum and the discrepancy with the Hipparcos distance would be reduced.

Finally, Fig. 26 shows the position of the binary components on the HR diagram. M_{bol} of the primary star is -4.13 , and, for the secondary, -0.44 . The primary star $\log T_{\text{eff}}$ (averaged over the visible photosphere) is 4.164; the corresponding secondary star quantity is 3.789. If the primary star were rotating synchronously, its bolometric magnitude would be -4.58 and the secondary star bolometric magnitude would be -0.74 . The corresponding $\log T_{\text{eff}}$ values would be 4.255 and 3.820. These bolometric magnitudes are for an observer for whom the

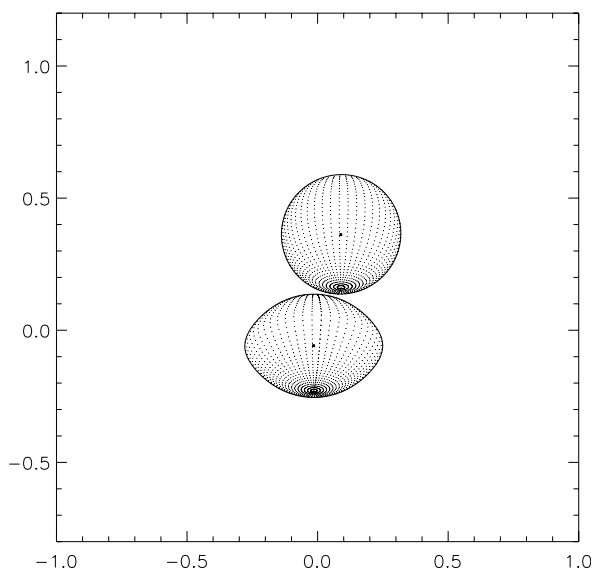


Fig. 22. View of V360 Lac model at orbital phase 0.98. The secondary star is nearer the observer. This view is associated with the spectra in Figs. 23 and 24.

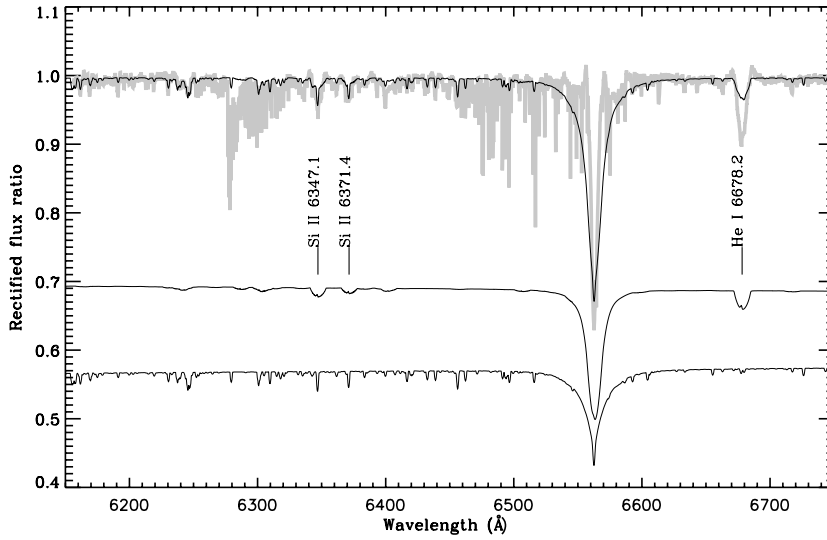


Fig. 23. Synthetic spectrum (thin line, top) compared with observed spectrum V3L10685 (grey curve) at orbital phase 0.98 (see Fig. 22). Spectra as in Fig. 17. Note the much greater depth of the H α absorption feature in the observed spectrum than at orbital phase 0.50, Fig. 20. The primary star spectrum has been positioned by adding -0.11 to all ordinates, and the secondary star spectrum has been positioned by adding 0.37 to all ordinates.

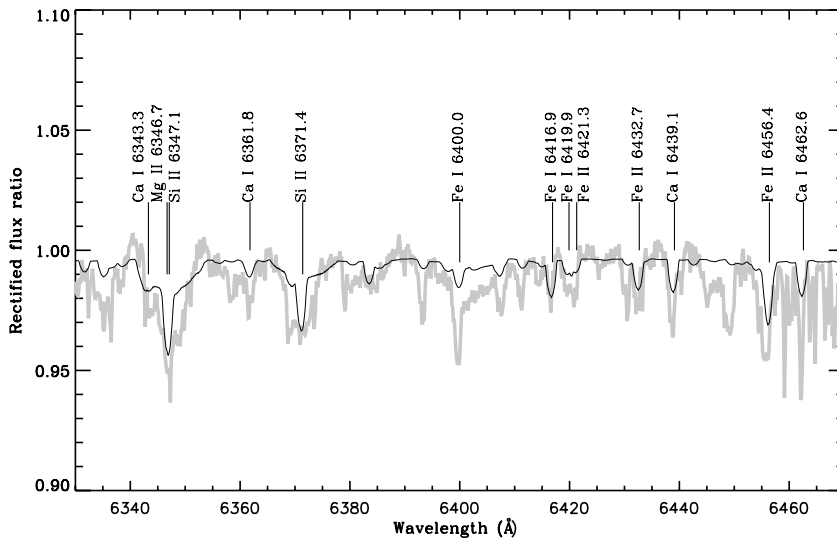


Fig. 24. Detail of Fig. 23. Note the differences from Fig. 21. The Si II emission wings are still present but the absorption component profiles are different from both Figs. 18 and 21.

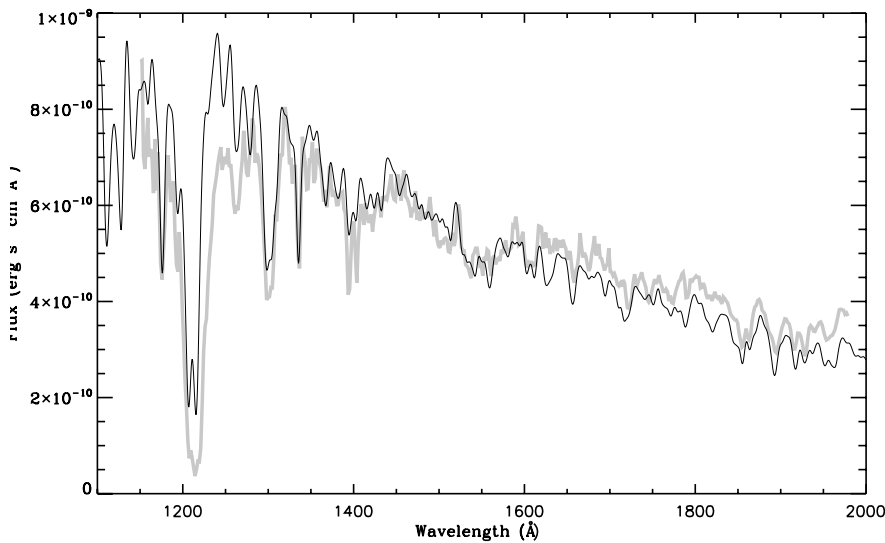


Fig. 25. Fit of synthetic spectrum (thin line) to IUE spectrum SWP09204 (grey curve). The synthetic spectrum has been divided by 2.5×10^{42} to superpose it on the IUE spectrum.

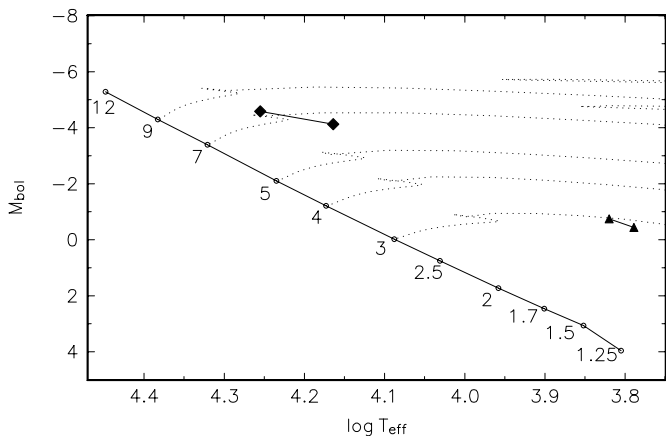


Fig. 26. Location of individual binary components on a main sequence HR diagram, marked by the heavy solid line, with ZAMS stellar masses indicated. The rightmost diamond marks the primary star as affected by rotation. The leftmost diamond marks the location of the primary star if it were rotating synchronously. The rightmost triangle marks the secondary, including irradiation by the rapidly rotating primary star. The leftmost triangle marks the secondary as it would be located if the primary were rotating synchronously. In the latter case the primary star is hotter, because of reduced gravitational darkening, and so irradiative heating of the secondary star is greater. The bolometric magnitudes are as evaluated by an observer for whom the orbital inclination is 65° .

orbital inclination is 65° . It is seen that the position of the primary roughly corresponds to its mass⁴ while the position of the secondary must obviously be a result of ongoing mass exchange in the system. That position cannot result from the evolution of a star with a mass only slightly larger than $1 M_\odot$.

8. A possible accretion disk model

In the present system we have shown that there is photometric (Sect. 3.2, 4.1), and spectroscopic (Sect. 4.2, Fig. 23) evidence for circumstellar material. An important point is that the $H\alpha$ emission lines follow the orbital motion of the primary star and show a strong absorption reversal at orbital phase 0.98, reasonably interpreted as evidence of a mass transfer stream. The rapid primary star rotation is most easily explained by mass transfer from the companion. It is not unreasonable to postulate that an accretion disk surrounds the primary star. The disk cannot be a standard accretion disk since the mass transfer stream impacts the primary star directly, according to Lubow & Shu (1975). (However, see the study by Kříž (1971).) A conjectural alternative is that the disk results from the splash of the mass transfer impact on the primary star. The rapid rotation of the primary star, with reduced equatorial gravity, facilitates this possibility. The potential well of the primary star is shallow and the disk must be cold, with a small viscosity (Frank et al. 1995) and corresponding long decay time against accretion onto the primary star. Once an accretion disk is formed, further mass transfer will impact the accretion disk, tending to maintain it.

The BINSYN package supports analysis of a system with an optically thick accretion disk. We have tested a large number of

possible models and found one which accurately represents all of the observational data. As with the system model of Table 6, the accretion disk model requires the primary star to rotate at critical rotation and its individual light curves to be affected by irradiation by the secondary star. The orbital inclination, in this model, is 70° and the primary star mass is $6.69 M_\odot$. In this model, secondary minimum is produced in part by eclipse of the primary star by the accretion disk, extending to the tidal cutoff radius.

A potentially serious objection to this model is that absorption lines might be expected in the spectra due to light from the primary star passing through the accretion disk, assumed to be partially transparent. Detailed calculations would be necessary to determine whether such absorption lines would be easily detectable. During secondary eclipse the obscured upper half of the primary star provides only 17% of that star's light at 5500 \AA . Absorption lines produced in the accretion disk will be broadened by Keplerian rotation, and those lines would appear on only a small fraction of the total flux from the primary star.

Without conclusive observational evidence in either direction, it is as likely that an accretion disk will be optically thin as optically thick. At the present time, the observational data demonstrate that circumstellar matter is present, but not enough data are available to constrain a system model.

9. Discussion and summary

The model presented in this paper depends strongly on the value of the mass ratio, q . We take the value $q = 0.163$, from the final solution, Table 6, as a fixed value not subject to empirical variation in the modelling process. Earlier attempts at a solution used a variety of q values. A system model for a given q value is a lengthy, computationally-intensive process. The solution is complicated by the absence of eclipses, which would permit application of more traditional light curve solution techniques. In the present instance, a formal optimization of parameters, either by differential corrections (Wilson & Devinney 1971; Linnell 1989) or by the simplex method (Kallrath & Linnell 1987), is not possible. Fits, for example, would be required to the rectified observed spectrum, by, say, χ^2 . This process would require a setup procedure that is not easily amenable to automation. We have simply used visual estimates for Fig. 14 to determine an acceptable fit. As we have seen in Sect. 7.2, the depths of the model Balmer lines depend on the rotation parameter FV_1 but not in a uniform way with the line sequence. The observed spectra show cycle-to-cycle variability that would seriously affect the optimization process. These complexities justify use of visual estimates in selecting a system model.

Because of the V360 Lac time-wise variations, both photometric and spectroscopic, the model derived in this paper represents a temporal average. Note that the conditions on the solution include agreement with Eq. (3), an acceptable fit to the *IUE* spectrum, fits to the other observed spectra, accurate representation of the radial velocity curves, and accurate fits to the *UBV* light curves.

Our principle results are:

(1) V360 Lac is a binary system in which the stellar masses are $7.45 \pm 0.3(\text{est})M_\odot$ (primary) and $1.21 \pm 0.05(\text{est})M_\odot$ (secondary). The orbital inclination is near 65° . Observed low amplitude *UBV* light curves severely constrain possible system models. There are no stellar eclipses.

(2) The primary star rotates at 6.19 times synchronous rate, corresponding to critical rotation. The primary star has a polar T_{eff} of 18 000 K. The secondary star fills its Roche lobe and has

⁴ Note that according to Maeder & Meynet (2000) rapid rotation does not change the position of a star in the HR diagram too much during its main-sequence stage, but its accurate observed position depends on the aspect effect (inclination). This is so because a star's effective temperature, originally defined in terms of spherical stars, is affected by local temperature variation over a distorted and irradiated photosphere.

a polar T_{eff} of 6000 K. V360 Lac is a new example of the morphological type termed “double-contact” by Wilson.

(3) Rapid rotation of the primary star, plausibly produced by mass transfer from the secondary, leads to reduced equatorial gravity. Associated gravity darkening produces a 9000 K lower equatorial T_{eff} than at the pole. The lower equatorial gravity permits detectable tidal distortion of the primary star by the secondary star as well as detectable irradiative heating by the secondary star.

(4) A variety of observations indicate the presence of circumstellar matter moving with the primary star.

(5) Synthetic spectra closely fit an *IUE* spectrum and accurately fit both blue and red rectified spectra. The synthetic spectra fully allow for gravity darkening and tidal and rotational distortion of both stellar components. The *IUE* spectrum fit indicates a system distance of approximately 500 pc, about 2σ beyond the Hipparcos distance.

Acknowledgements. We acknowledge the use of Hadrava’s programs KOREL and FOTEL and thank Dr. Hadrava for his advice how to use KOREL in more complicated situations. The use of the computerized bibliography from the Strasbourg Astronomical Data Centre is also gratefully acknowledged. Research of PH and MW was supported from the research plan J13/98: 113200004 of Ministry of Education, Youth and Sports. P. Harmanec, P. Koubský P. Škoda and M. Šlechta were also supported from the research plans AV OZ1 003909, 0030501 and project K2043105 of the Academy of Sciences of the Czech Republic. At later stages, this research was supported from the grants GA ČR 102/02/1000, GA ČR 205/03/0788 and GA ČR 205/06/0304 of the Granting Agency of the Czech Republic. The stay of PK at DAO was supported by a grant through the NATO Science Fellowship Programme. PH, PE, MW and JL also acknowledge the support from the Czech-Mexican KONTAKT ME402(2000)/CONACyT E130.734 collaborative project. We thank the anonymous referee for extensive comments which greatly improved the presentation of this paper.

References

- Becker, W. in Basic Astronomical Data, Stars and Stellar Systems Vol. III, (Chicago: Univ. of Chicago Press) ed. K. A. Strand, 241
- Bossi, M., et al. 1998, *A&AS*, 127, 433
- Claret, A. 2001, *MNRAS*, 327, 989
- Cox, A. N. 2000, *Allen’s Astrophysical Quantities* (New York: Springer)
- Cranmer, S. R. 2005, *Astrophysical Journal*, 634, 2005
- Frank, J., King, A., & Raine, D. 1995, in *Accretion Power in Astrophysics*, 2d edn. (Cambridge: Univ. Press)
- Frémat, Y., Zorec, J., Hubert, A.-M., & Floquet, M. 2005, *A&A*, 440, 305
- Geary, A. E., & Richards, M. T. 1996, *ApJ*, 459, L99
- Hadrava, P. 1990, *Contr. Astron. Obs. Skalnaté Pleso*, 20, 23
- Hadrava, P. 1995, *A&AS*, 114, 393
- Hadrava, P. 1997, *A&AS*, 122, 581
- Hadrava, P. 2004a, *Publ. Astron. Inst. Acad. Sci. Czech Rep.*, 92, 1
- Hadrava, P. 2004b, *Publ. Astron. Inst. Acad. Sci. Czech Rep.*, 92, 15
- Harmanec, P. 1988, *Bull. Astron. Inst. Czechosl.*, 39, 329
- Harmanec, P. 1998, *A&A*, 335, 173
- Harmanec, P. 2001, *Publ. Astron. Inst. Acad. Sci. Czech Rep.*, No. 89, 9
- Harmanec, P. 2002, in *ASP Conf. Ser.*, 279, 221
- Harmanec, P. 2003, in *New Directions for Close Binary Studies: The Royal Road to the Stars*, *Publ. Canakkale Onsekiz Mart Univ.* 3, Canakkale, Turkey, 221
- Harmanec, P., Horn, J., & Juza, K. 1994, *A&AS*, 104, 121
- Harmanec, P., & Horn, J. 1998, *Journal of Astronomical Data*, 4, CD-ROM file 5
- Hill, G., Harmanec, P., Pavlovski, K., et al. 1997, *A&A*, 324, 965 (paper 17)
- Horn, J., Kubát, J., Harmanec, P., et al. 1996, *A&A*, 309, 521
- Hubeny, I., Štefl, S., & Harmanec, P. 1985, *Bull. Astron. Inst. Czech.*, 36, 214
- Johnson, H. L., Iriarte, B., Mitchell, R. I., & Wisniewski, W. Z. 1966, *CoLPL*, 5, 99
- Kallrath, J., & Linnell, A. P. 1987, *ApJ*, 313, 346
- Kaufer, A., Stahl, O., Wolf, B., et al. 1996, *A&A*, 314, 599
- Kříž, S. 1971, *BAC*, 22, 108
- Kurucz, R. L. 1993b, *Solar Abundance Model Atmospheres*, Kurucz CD-ROM No. 19
- Limber, D. N. 1963, *ApJ*, 139, 1112
- Linnell, A. P. 1984, *ApJS*, 54, 17
- Linnell, A. P. 1989, *ApJ*, 342, 449
- Linnell, A. P., & Hubeny, I. 1996, *ApJ*, 471, 958
- Lubow, S. H., & Shu, F. H. 1975, *ApJ*, 198, 383
- Maeder, A., & Meynet, G. 2000, *ARA&A*, 38, 143
- Massa, D., & Fitzpatrick, E. L. 2000, *ApJS*, 126, 517
- Pavlovski, K., Harmanec, P., Božić, H., et al. 1997, *A&AS*, 125, 75
- Perryman, M. A. C., Høg, E., Kovalevsky, J., Lindegren, L., & Turon, C. 1997, *ESA SP-1200: The Hipparcos and Tycho Catalogues*
- Porter, J. M., & Rivinius, T. 2003, *PASP*, 115, 1153
- Richards, M. T., Koubský, P., Šimon, V., et al. 2000, *ApJ*, 531, 1003
- Savage, B. D., & Mathis, J. S. 1979, *ARA&A*, 17, 73
- Škoda, P. 1996, in *Astronomical Data Analysis Software and Systems V*, ed. G. H. Jacoby, & J. Barnes, *ASP Conf. Ser.*, 101, 187
- Škoda, P., & Šlechta, M. 2002, *Publ. Astron. Inst. Acad. Sci. Czech Rep.*, 90, 40
- Šlechta, M., & Škoda, P. 2002, *Publ. Astron. Inst. Acad. Sci. Czech Rep.*, 90, 1
- Struve, O. 1931, *ApJ*, 73, 94
- Tassoul, J.-L. 1978, *Theory of Rotating Stars* (Princeton: Univ. Press), Ch. 8
- Townsend, R. H. D., Owocki, S. P., & Howarth, I. D. 2004, *MNRAS*, 350, 189
- Vondrák, J. 1969, *Bull. Astron. Inst. Czechosl.*, 20, 349
- Vondrák, J. 1977, *Bull. Astron. Inst. Czechosl.*, 28, 84
- Wade, R. A., & Rucinski, S. M. 1985, *A&AS*, 60, 471
- Wilson, R. E. 1979, *ApJ*, 234, 1054
- Wilson, R. E. 1990, *ApJ*, 356, 613
- Wilson, R. E. 1994, *PASP*, 106, 921
- Wilson, R. E., & Devinney, E. J. 1971, *ApJ*, 166, 605
- Wilson, R. E., Van Hamme, W., & Pittera, L. E. 1985, *ApJ*, 289, 748